

# The interplay between activity and filament flexibility determines the emergent properties of active nematics

Abhijeet Joshi,<sup>\*</sup> Elias Putzig, Aparna Baskaran,<sup>†</sup> and Michael F. Hagan<sup>‡</sup>  
*Martin Fisher school of Physics, Brandeis University, Waltham, MA 02453, USA*

(Dated: September 5, 2018)

Active nematics are microscopically driven liquid crystals that exhibit dynamical steady states characterized by the creation and annihilation of topological defects. Motivated by experimental realizations of such systems made of biopolymer filaments and motor proteins, we describe a large-scale simulation study of a particle-based computational model that explicitly incorporates the semiflexibility of the biopolymers. We find that energy injected into the system at the particle scale preferentially excites bend deformations, renormalizing the filament bend modulus to smaller values. The emergent characteristics of the active nematic depend on activity and flexibility only through this activity-renormalized bend modulus, demonstrating that material parameters such as the Frank ‘constants’ must explicitly depend on activity in a continuum hydrodynamic description of an active nematic. Further, we present a systematic way to estimate these material parameters from observations of deformation fields and defect shapes in experimental or simulation data.

Active nematics are a class of non-equilibrium liquid crystalline materials in which the constituent particles transduce energy into stress and motion, driving orientationally inhomogeneous dynamical steady states characterized by generation, annihilation, and streaming of topological defects [1–6]. Being intrinsically far-from-equilibrium, active nematics enable developing materials with capabilities that would be thermodynamically forbidden in an equilibrium system. However, such applications require understanding how an active nematic’s macroscale material properties depend on the microscale features of its constituent nematogens.

The challenge in this task can be illustrated by considering the shape of a defect. Defects have been the subject of intense research in equilibrium nematics, since they must be eliminated for display technologies, and controlled for applications such as directed assembly and biosensing [7–9]. Theory and experiments [9–11] have shown that defect morphologies depend on the relative values of the bend and splay elastic moduli,  $k_{33}$  and  $k_{11}$  (Fig. 1a), defined in the Frank free energy density for a 2D nematic as  $f_F = k_{11} (\nabla \cdot \hat{n})^2 + k_{33} (\hat{n} \times (\nabla \times \hat{n}))^2$  with  $\hat{n}$  the director field [12, 13]. Different experimental realizations of active nematics also exhibit variations in defect morphologies (*e.g.* Fig. 1c and Fig. 1d). However, relating these defect morphologies to material constants is much less straightforward than in equilibrium systems. Since moduli cannot be rigorously defined in a non-equilibrium system such as an active nematic, there is no systematic way to measure them.

Computational and theoretical modeling could overcome these limitations. Symmetry-based hydrodynamic theories [14–16] have led to numerous insights about active nematics, including describing defect dynamics

(*e.g.* [17–21]), induced flows in the suspending fluid (*e.g.* [22, 23]), and how confinement in planar [24–26] and curved geometries [27–30] controls defect proliferation and dynamics. However, hydrodynamic theories cannot predict how material constants or emergent behaviors depend on the microscale properties of individual nematogens. Further, while simulations of active nematics composed of rigid rods [2, 31, 32] have elucidated emergent morphologies, these models do not account for internal degrees of freedom available to flexible nematogens [1, 33, 34].

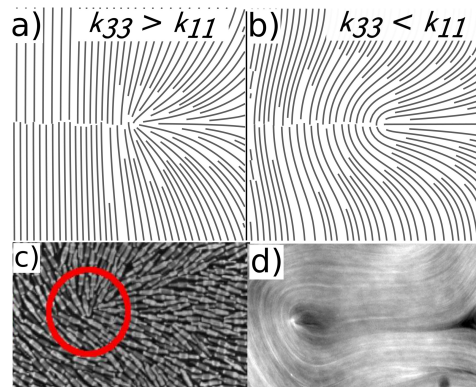


FIG. 1. (a,b) The equilibrium director field configuration near a  $+\frac{1}{2}$  defect for (a) bend modulus larger than splay modulus  $k_{33}/k_{11} = 3.4$ , leading to pointed defects and (b) splay modulus larger than bend  $k_{33}/k_{11} = 0.3$  leading to rounded defects. In each case the director field was calculated by numerically minimizing the Frank free energy around a separated  $\pm\frac{1}{2}$  defect pair. (c,d) Typical defect morphologies observed in (c) a vibrated granular nematic [5] and (d) a microtubule-based active nematic [1, 35].

In this work, we perform large-scale simulations on a model active nematic composed of semiflexible filaments, and determine how its emergent morphology depends on filament stiffness and activity. Fig. 2 shows representative simulation outcomes. We find that character-

<sup>\*</sup> email:aa.joshi@brandeis.edu

<sup>†</sup> email:aparna@brandeis.edu

<sup>‡</sup> email:hagan@brandeis.edu

istics of the active nematic texture — the defect density, magnitudes and characteristic scales of bend and splay deformations, the shape of motile  $+\frac{1}{2}$  defects, and number fluctuations — can all be described as functions of an ‘activity-renormalized’ nematogen rigidity,  $\kappa_{\text{eff}} \cong \kappa/(f^a)^2$ , where  $\kappa$  is the intrinsic bending modulus of the nematogen and  $f^a$  is a measure of its activity. We show that one can define effective bend and splay moduli analogous to their equilibrium counterparts, but that the bend modulus is proportional to  $\kappa_{\text{eff}}$ . Thus, activity leads to an apparent softening of the nematic. This observation demonstrates that activity preferentially dissipates into particular modes within an active material, depending on the internal degrees of freedom of its constituent units. Moreover, these results suggest revisiting assumptions underlying hydrodynamic theories of active matter; for instance material parameters should explicitly depend on activity.

We also present a method of parameterizing defect shapes, which enables estimating the relative magnitudes of renormalized bend and splay constants from experimental observations of defects, and thus allows direct experimental testing of our prediction.

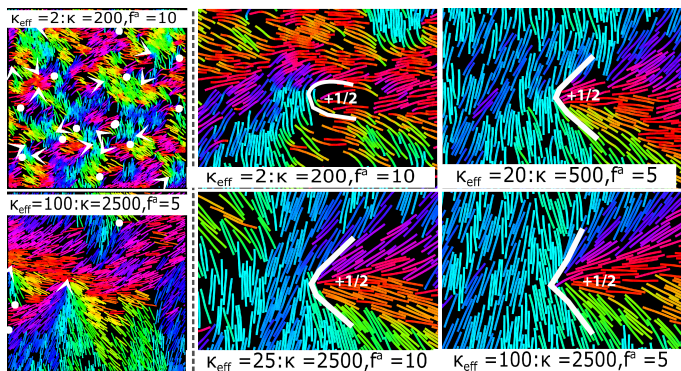


FIG. 2. A visual summary of how active nematic emergent properties depend on the activity parameter  $f^a$  and the filament modulus  $\kappa$ . The left panel in each row shows  $1/16^{\text{th}}$  of the simulation box for indicated parameter values, with white arrows indicating positions and orientations of  $+\frac{1}{2}$  defects and white dots indicating positions of  $-\frac{1}{2}$  defects. Filament beads are colored according to the orientations of the local tangent vector. The right 4 panels are each zoomed in on a  $+\frac{1}{2}$  defect, with indicated parameter values. The white lines are drawn by eye to highlight defect shapes. Animations of corresponding simulation trajectories are in [36].

*Model.* We seek a minimal computational model that captures the key material properties and symmetries of active nematics, namely extensile activity, nematic interparticle alignment and semiflexibility. We model active filaments as semiflexible bead-spring polymers, each containing  $M$  beads of diameter  $\sigma$ , with neighboring beads connected by finitely extensible (FENE) bonds [37], and flexibility controlled by a harmonic angle potential between successive bonds that sets the filament bending modulus  $\kappa$ . Activity is implemented as a force of mag-

nitude  $f^a$  acting on each filament bead along the local tangent to the filament. To make activity nematic, the active force on every bead within a given filament reverses direction after a time interval chosen from a Poisson distribution with mean  $\tau_1$ . Each bead is further subject to an isotropic stochastic white noise. Further model details are in Section S2 of [36]. The Langevin equations governing the system dynamics were integrated using a modified version of LAMMPS [38]. The model combines features of recent models for polar self-propelled polymers [39] and the reversing rods approach to rigid active nematic rods [32].

Since we are motivated by systems sufficiently large that boundary effects are negligible (*e.g.* Ref. [2]), we performed simulations in a  $A = 840 \times 840\sigma^2$  periodic simulation box, with  $N = 19404$  filaments, each with  $M = 20$  beads, so that the packing fraction  $\phi = MN\sigma^2/A \approx 0.55$ . Fixing all other model parameters, we varied the filament stiffness,  $\kappa \in [10^2, 10^4]k_B T_{\text{ref}}$  and the magnitude of the active force,  $f^a \in [5, 30]k_B T_{\text{ref}}/\sigma$ , where the units are set by the thermal energy at a reference state  $k_B T_{\text{ref}}$ , and the filament diameter  $\sigma$ . We initialized the system by first placing the filaments in completely extended configurations, on a rectangular lattice with filaments oriented along one of the lattice vectors. We then relaxed the initial configuration for  $10^4\tau$  (by which point the defect density saturated for all parameter sets), where  $\tau = \sqrt{m\sigma^2/k_B T_{\text{ref}}}$ , before performing production runs of  $\sim 4 \times 10^4\tau$ . In the limit of high stiffness or low activity, the unphysical crystalline initial condition did not relax on computationally accessible timescales. In these cases, we used an alternative initial configuration, with filaments arranged into four rectangular lattices, each placed in one quadrant of the simulation box such that adjacent (non-diagonal) lattices were orthogonal.

We analyzed simulation trajectories by calculating the local nematic tensor  $Q_{\alpha\beta}$  and the density field  $\rho$  on a  $1000 \times 1000$  grid. We then evaluated the local nematic order parameter  $S$  and director  $\hat{n}$  as the largest eigenvalue of  $Q$  and corresponding eigenvector [40]. We determined defect locations and orientations following standard approaches; further details are in Section S9 of [36]. We could not measure defect densities for systems with  $f^a \geq 20$  and  $\kappa \gtrsim 5000$  because these systems exhibit localized density fluctuations which cause the detection algorithm to break down.

*Results.* To understand how the interplay between filament flexibility and activity determines the texture of an active nematic, let us first consider the basic physics governing the emergent phenomenology in our system. Deforming a nematogen causes an elastic stress that scales  $\sim \kappa$ , the filament bending modulus. This elastic stress must be balanced by stresses arising from interparticle collisions. These collisional stresses have two contributions. First there are the passive collisional stresses, which are  $\mathcal{O}(1)$  in our units (as we have chosen the thermal energy and the particle size  $\sigma$  as the energy and length scales). Then there are active collisional stresses

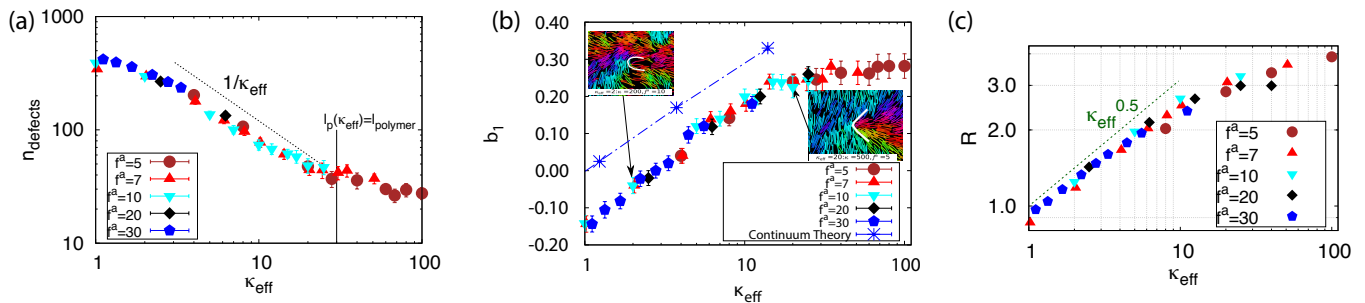


FIG. 3. The characteristics of an active nematic are determined by the renormalized bending rigidity,  $\kappa_{\text{eff}} = \kappa/(f^a)^2$ . (a) The average number of defects  $n_{\text{defect}}$  observed in steady states as a function of  $\kappa_{\text{eff}}$ , for activity parameter values  $f^a \in [5, 30]$  and  $\kappa \in [100, 3000]$ . (b) Mode of defect shape parameter  $b_1$  for  $+\frac{1}{2}$  defects as a function of  $\kappa_{\text{eff}}$  for  $f^a \in [7, 30]$  and  $\kappa \in [100, 10000]$ , with  $b_1(r)$  values evaluated at a radial distance  $r = 12.6\sigma$  from the defect core. The dashed line and blue asterisk symbols show values of  $b_1$  calculated for isolated defects from equilibrium continuum elastic theory, with the ratio of bend and splay moduli  $k_{33}/k_{11}$  for each  $\kappa_{\text{eff}}$  set according to the measured ratio  $R$  of bend and splay deformations in (c). (c) The ratio of splay and bend deformations,  $R = \langle \int d^2\mathbf{r} D_{\text{splay}}(\mathbf{r}) \rangle / \langle \int d^2\mathbf{r} D_{\text{bend}}(\mathbf{r}) \rangle$  as a function of  $\kappa_{\text{eff}}$  for the same parameters as in (b). The simulation box size is  $(840 \times 840\sigma^2)$  for all cases. Explicit parameter values for each symbol are shown in Fig. S2 [36].

that arise due to the self-replenishing active force of magnitude  $f^a$  acting on each monomer. The active collisional stress will scale as  $\nu_{\text{coll}} \Delta p_{\text{coll}}$ , i.e., the collision frequency times the momentum transfer at each collision. Both the collision frequency and momentum transfer will scale with the self-propulsion velocity [41], which in our model is set by  $f^a$ . Thus, the collisional stresses will scale  $\sim (1 + (f^a)^2)$ . So, the system properties will be controlled by a parameter which measures the ratio of elastic to collisional stresses,  $\kappa_{\text{eff}} \equiv \kappa/(1 + (f^a)^2)$ . Because we focus on the moderate to large activity regime, the passive stresses are negligible and we set  $\kappa_{\text{eff}} \approx \kappa/(f^a)^2$ .

We now test this argument against our simulation results, using several metrics for deformations in the nematic order: defect density, defect shape, and the distribution of energy in splay and bend deformations. As shown in Fig. 3, all of these quantities depend on bending rigidity and activity only through the combination  $\kappa_{\text{eff}}$ .

**Defect Density:** We first test this argument in the context of a well-studied property of an active nematic, the steady-state defect density [18, 22, 25, 42]. Fig. 3a plots the defect density for a range of microscopic flexibility and activity values. The data collapses into a single curve, substantiating the arguments above. Data collapse breaks down for  $f^a < 5$  (Fig. S1 [36]) when the system loses nematic order (see below). The defect density roughly scales as  $1/\kappa_{\text{eff}}$  under parameter values for which the renormalized persistence length lies between the monomer scale and filament contour length,  $1.5 \lesssim \kappa_{\text{eff}} \lesssim \kappa_{\text{eff}}^{\text{max}}$ , with  $\kappa_{\text{eff}}^{\text{max}} \approx 30$ . While longer filaments would be required to rigorously test the scaling of defect density with  $\kappa_{\text{eff}}$ , we found the same dependence over a wider parameter range by estimating the persistence length from filament tangent fluctuations (Fig. S3, [36]), and we observe the same scaling for an additional data set (Fig. S1 [36]). Hydrodynamic theories such as [18, 22, 25, 42] predict that the defect density scales as  $\alpha/K$ , where  $\alpha$  is the measure of active stress in the hy-

drodynamic theories and  $K$  is a Frank elastic constant. The scaling collapse observed in our simulations indicates that these hydrodynamic parameters are directly related to their microscopic analogs, namely the filament elastic constant  $\kappa$  and the collisional active stress  $\sim (1 + (f^a)^2)$ .

**Defect Shape:** Let us now consider a striking feature of the texture of an active nematic, the shape of a  $+\frac{1}{2}$  defect. A quantitative descriptor of defect shape can be developed as follows. We choose a coordinate system with its origin at the center of the defect core, with the  $x$ -axis pointing along the defect orientation (see Fig. S13 in [36]). We work in polar coordinates, with  $r$  the radial distance from the defect core and  $\phi$  as the azimuthal angle with respect to the  $x$ -axis. We define  $\theta$  as the angle of the director field with respect to the  $x$ -axis. At any position, we can then express  $\theta(r, \phi)$  as a Fourier expansion in  $\phi \in \{-\pi : \pi\}$ . However, in practice truncating the expansion after the first sin term approximates the shape of a  $+\frac{1}{2}$  defect well, so the descriptor simplifies to  $\theta_{+\frac{1}{2}}(r, \phi) \approx \frac{1}{2}\phi + b_1(r) \sin(\phi)$ , and the result is insensitive to  $r$  provided the measurement is performed outside of the defect core (see Fig. S14 [36]). Thus, the parameter  $b_1$  uniquely describes the defect shape; in particular, larger values of  $b_1$  correspond to pointier defects. Note that Zhang et al. [11] and Cortese et al. [21] proposed similar approaches to characterizing defect shapes while we were preparing this manuscript. An advantage of our approach is that the shape can be described by a single number,  $b_1$ .

Figure 3b shows the mode of  $b_1$  calculated from defects within our simulations depends only on  $\kappa_{\text{eff}}$ , thus demonstrating that defect shape is controlled by the renormalized bending rigidity. Moreover,  $b_1$  increases logarithmically with  $\kappa_{\text{eff}}$ ; i.e., defects become more pointed as the bending rigidity increases, consistent with the previous observations of highly pointed defects in rigid rod simulations [2, 31, 43].

**Splay and Bend deformations:** Next, to characterize



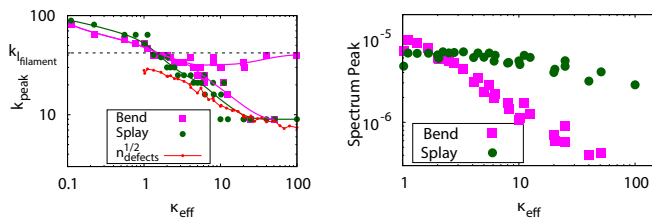


FIG. 4. Analysis of the power spectra of splay and bend deformation energy densities: **(a)** The wavenumbers corresponding to peaks  $k_{\text{peak}}$  in bend (■ symbols) and splay (● symbols) power spectra, and the inverse defect spacing,  $\sqrt{\langle n_{\text{defect}} \rangle}$  (● symbols) as functions of  $\kappa_{\text{eff}}$ . The predominant scale of splay deformations transitions from the individual filament scale ( $k_{\text{filament}}$ , dashed line) at low  $\kappa_{\text{eff}}$  to the defect spacing scale at high  $\kappa_{\text{eff}}$ . Bend spectra exhibit two peaks, corresponding to filament and defect-spacing scales, for high  $\kappa_{\text{eff}}$ . **(b)** The maximum magnitude of the power spectra, showing that splay is insensitive to  $\kappa_{\text{eff}}$  while bend deformations decrease in magnitude until the effective rigidity exceeds the filament length.

the overall texture of the active nematic, we consider the deformations in its order field. In a 2D nematic, any arbitrary deformation of the director field can be decomposed into a bend deformation  $\mathbf{d}_{\text{bend}} = (\hat{n}(\mathbf{r}) \times (\nabla \times \hat{n}(\mathbf{r})))$  and a splay deformation  $d_{\text{splay}} = (\nabla \cdot \hat{n}(\mathbf{r}))$ . We define associated strain energy densities  $D_{\text{bend}} = \rho S^2 |\mathbf{d}_{\text{bend}}|^2$  and  $D_{\text{splay}} = \rho S^2 d_{\text{splay}}^2$ , which measure how the system's elastic energy distributes into the two linearly independent deformation modes. The prefactors of density  $\rho$  and order  $S$  allow the definition to be valid in regions such as defect cores and voids that occur in the particle simulations.

To assess  $\kappa_{\text{eff}}$  as the analog of an equilibrium modulus, let us consider the ratio of total strain energy in splay deformations to those in bend,  $R = \langle \int d^2\mathbf{r} D_{\text{splay}}(\mathbf{r}) \rangle / \langle \int d^2\mathbf{r} D_{\text{bend}}(\mathbf{r}) \rangle$ . In equilibrium, equipartition requires that this ratio satisfy  $R_{\text{eq}} = k_{33}/k_{11}$ . In our simulations we observe data collapse for all parameter sets, with the ratio roughly scaling as  $R \sim \kappa_{\text{eff}}^{1/2}$  (Fig. 3c). This result supports the existence of effective elastic moduli in an active nematic, but again shows that their values are activity-dependent. Note that this differs from the scaling of an equilibrium nematic, where the moduli scale as  $k_{33} \sim \kappa$  and  $k_{11} \sim \kappa^{1/3}$  [44, 45], giving  $R_{\text{eq}} \sim \kappa^{2/3}$ . We confirmed this scaling by calculating the equilibrium moduli for our system (Fig. S7 [36]) using the free energy perturbation technique of [46].

Analysis of simulation trajectories suggests that the difference in scaling arises because the active systems have much higher nematic order than the equilibrium systems (when compared at the same values of renormalized bending rigidity). In an equilibrium system, increasing the filament flexibility decreases order, resulting in a transition from the nematic to isotropic phase as  $\kappa$  decreases below 5 at the density used in our simulations [47]. In contrast, the active systems remain deep within

the nematic phase ( $S \gtrsim 0.8$ ) for all parameter sets (Fig. S7c in [36]). We empirically found that normalizing the bend-splay ratio by the degree of order, using the form  $R/S^2$ , roughly collapses the equilibrium and active results onto a single curve (Fig. S7b [36]). Although we cannot rationalize the form of the normalization, this result implies that the differences in scaling between active and equilibrium cases arise from the increased nematic order in the active simulations.

The power spectra associated with these strain energies (Fig. S6 in [36]) exhibit two features: a) Fig. 4a shows that for the smallest simulated effective rigidity,  $\kappa_{\text{eff}} = 2$ , the peak of the power spectrum  $k_{\text{peak}}$  is on the filament scale, indicating that most deformation energy arises due to bending of individual filaments. But for all higher values of  $\kappa_{\text{eff}}$ , a peak arises at the defect spacing scale, indicating that the defect density controls the texture in this active nematic. b) Fig. 4b shows the magnitude of the power spectrum at the characteristic scale  $k_{\text{peak}}$ . The splay energy density is nearly independent of the effective filament stiffness, while the amount of bend decreases linearly with  $\kappa_{\text{eff}}$  (for  $\kappa_{\text{eff}} \lesssim \kappa_{\text{eff}}^{\text{max}}$ ). This observation further supports  $\kappa_{\text{eff}}$  as an effective bend modulus, and demonstrates that energy injected into the system at the microscale due to activity preferentially dissipates into bend modes.

Returning to the defect shape analysis, the dashed line in Fig. 3b shows the defect shape parameter values  $b_1$  calculated by minimizing the continuum Frank free energy for an equilibrium system containing a separated pair of  $+\frac{1}{2}$  and  $-\frac{1}{2}$  defects. Here we have fixed the continuum modulus  $k_{11}$  and varied  $k_{33}$  so that  $R_{\text{eq}} = \frac{k_{33}}{k_{11}}$  matches the value obtained from our microscopic simulations at the corresponding value of effective stiffness:  $R_{\text{eq}}(k_{33}) = R(\kappa_{\text{eff}})$ . Although the equilibrium  $b_1$  values are shifted above the simulation results, consistent with the discrepancy in  $R$  between the active and passive systems (Fig. 3C and Fig. S7 [36]), we observe the same scaling with bending rigidity in the continuum and simulation results. Thus, the defect shape measurement provides a straightforward means to estimate effective moduli in simulations or experiments on active nematics.

Finally, previous work has shown that active nematics are susceptible to phase separation [32, 48–50] and giant number fluctuations [5, 48, 51–53]. We find that the renormalized modulus governs the latter, with deviations from equilibrium scaling roughly proportional to  $\kappa_{\text{eff}}$ . However, flexibility suppresses phase separation except at molecular scales (Fig. S11 [36]).

*Conclusions.* In active materials, energy injected at the particle scale undergoes an inverse cascade, manifesting in collective spatiotemporal dynamics at larger scales. The nature of this emergent behavior depends crucially on which modes the active energy dissipates into. Our simulations show that activity within a dry active nematic preferentially dissipates into bend modes, thus softening the apparent bend modulus. This renor-

malized bend modulus dictates all collective behaviors that we investigated — the relative amounts of bend and splay, defect density, defect shape, and giant number fluctuations. The dependence of multiple characteristics on this single parameter suggests that bend and splay moduli can be meaningfully assessed in an active nematic, despite the fact that there is no rigorous definition for a modulus in a non-equilibrium active material. Finally, our technique to parameterize defect shapes allows estimating the relative magnitudes of these effective moduli in any experimental or computational system that exhibits defects.

## ACKNOWLEDGMENTS

This work was supported by the Brandeis Center for Bioinspired Soft Materials, an NSF MRSEC, DMR-1420382 (AJ,EP,AB,MFH) and NSF DMR-1149266 (AB). Computational resources were provided by NSF XSEDE computing resources (MCB090163, Stampede) and the Brandeis HPCC which is partially supported by DMR-1420382.

- 
- [1] T. Sanchez, D. T. N. Chen, S. J. Decamp, M. Heymann, and Z. Dogic, *Nature* **491**, 431434 (2012), arXiv:1301.1122.
- [2] S. J. DeCamp, G. S. Redner, A. Baskaran, M. F. Hagan, and Z. Dogic, *Nat. Mater.* **14**, 1110 (2015).
- [3] C. Peng, T. Turiv, Y. Guo, Q.-H. Wei, and O. D. Lavrentovich, *Science* **354**, 882 (2016).
- [4] S. Zhou, A. Sokolov, O. D. Lavrentovich, and I. S. Aranson, *Proc. Natl. Acad. Sci. U. S. A.* **111**, 1265 (2014), <http://www.pnas.org/content/111/4/1265.full.pdf>.
- [5] V. Narayan, S. Ramaswamy, and N. Menon, *Science* **317**, 105 (2007).
- [6] V. Narayan, N. Menon, and S. Ramaswamy, *J. Stat. Mech: Theory Exp.* **2006**, P01005 (2006).
- [7] D. J. Broer, *Nat. Mater.* **9**, 99 (2010).
- [8] I.-h. Lin, D. S. Miller, P. J. Bertics, C. J. Murphy, J. J. de Pablo, and N. L. Abbott, *Science* **332**, 1297 (2011).
- [9] M. Kleman, *Rep. Prog. Phys.* **52**, 555 (1989).
- [10] S. Zhou, S. V. Shiyankovskii, H.-S. Park, and O. D. Lavrentovich, *Nat. Commun.* **8**, 14974 (2017).
- [11] R. Zhang, N. Kumar, J. L. Ross, M. L. Gardel, and J. J. de Pablo, *Proc. Natl. Acad. Sci. U. S. A.* **115**, E124 (2018), <http://www.pnas.org/content/115/2/E124.full.pdf>.
- [12] F. C. Frank, *Discuss. Faraday Soc.* **25**, 19 (1958).
- [13] C. W. Oseen, *Trans. Faraday Soc.* **29**, 883 (1933).
- [14] R. A. Simha and S. Ramaswamy, *Phys. Rev. Lett.* **89**, 058101 (2002).
- [15] M. C. Marchetti, J. F. Joanny, S. Ramaswamy, T. B. Liverpool, J. Prost, M. Rao, and R. A. Simha, *Rev. Mod. Phys.* **85**, 1143 (2013), arXiv:1207.2929.
- [16] S. Ramaswamy, *Annu. Rev. Condens. Matter Phys.* **1**, 323 (2010), arXiv:1004.1933.
- [17] L. Giomi, M. J. Bowick, X. Ma, and M. C. Marchetti, *Phys. Rev. Lett.* **110**, 228101 (2013).
- [18] L. Giomi, M. J. Bowick, P. Mishra, R. Sknepnek, and M. Cristina Marchetti, *Phil. Trans. R. Soc. A* **372**, 20130365 (2014).
- [19] A. Doostmohammadi, T. N. Shendruk, K. Thijssen, and J. M. Yeomans, *Nat. Comm.* **8**, 15326 (2017), arXiv:1607.01376.
- [20] A. U. Oza and J. Dunkel, *New J. Phys.* **18**, 093006 (2016), arXiv:1507.01055.
- [21] D. Cortese, J. Eggers, and T. B. Liverpool, *Phys. Rev. E* **97**, 022704 (2018).
- [22] S. P. Thampi, R. Golestanian, and J. M. Yeomans, *EPL (Europhysics Letters)* **105**, 18001 (2014), arXiv:1312.4836.
- [23] L. Giomi, *Phys. Rev. X* **5**, 031003 (2015).
- [24] T. N. Shendruk, A. Doostmohammadi, K. Thijssen, and J. M. Yeomans, *Soft Matter* **13**, 3853 (2017).
- [25] M. M. Norton, A. Baskaran, A. Opathalage, B. Langeslay, S. Fraden, A. Baskaran, and M. F. Hagan, *Phys. Rev. E* **97**, 012702 (2018).
- [26] T. Gao, M. D. Betterton, A.-S. Jhang, and M. J. Shelley, *Phys. Rev. Fluids* **2**, 093302 (2017).
- [27] F. C. Keber, E. Loiseau, T. Sanchez, S. J. DeCamp, L. Giomi, M. J. Bowick, M. C. Marchetti, Z. Dogic, and A. R. Bausch, *Science* **345**, 1135 (2014), arXiv:15334406.
- [28] R. Zhang, Y. Zhou, M. Rahimi, and J. J. De Pablo, *Nat. Comm.* **7**, 13483 (2016).
- [29] P. W. Ellis, D. J. G. Pearce, Y.-W. Chang, G. Goldsztein, L. Giomi, and A. Fernandez-Nieves, *Nature Physics* **14**, 85 (2017).
- [30] F. Alaimo, C. Köhler, and A. Voigt, *Sci. Rep.* **7**, 5211 (2017), arXiv:1703.03707.
- [31] T. Gao, R. Blackwell, M. A. Glaser, M. D. Betterton, and M. J. Shelley, *Phys. Rev. Lett.* **114**, 048101 (2015), arXiv:1401.8059.
- [32] X.-q. Shi and Y.-q. Ma, *Nat. Comm.* **4**, 3013 (2013).
- [33] Y. Sumino, K. H. Nagai, Y. Shitaka, D. Tanaka, K. Yoshikawa, H. Chaté, and K. Oiwa, *Nature* **483**, 448 (2012).
- [34] P. Guillamat, J. Igns-Mullol, and F. Sagus, *Proc. Natl. Acad. Sci. U. S. A.* **113**, 5498 (2016), <http://www.pnas.org/content/113/20/5498.full.pdf>.
- [35] Image provided by Linnea Metcalf, Achini Opathalage and Zvonimir Dogc and used with their permission.
- [36] Supplementary material to this paper is provided at [URL].
- [37] K. Kremer and G. S. Grest, *J. Chem. Phys.* **92**, 5057 (1990), <http://dx.doi.org/10.1063/1.458541>.
- [38] S. Plimpton, *J. Comput. Phys.* **117**, 1 (1995).
- [39] K. R. Prathyusha, S. Henkes, and R. Sknepnek, *Phys. Rev. E* **97**, 022606 (2018).
- [40] R. Eppenga and D. Frenkel, *Mol. Phys.* **52**, 1303 (1984).
- [41] A. Baskaran and M. C. Marchetti, *Phys. Rev. Lett* **101**, 268101 (2008).
- [42] E. Putzig, G. S. Redner, A. Baskaran, and A. Baskaran, *Soft Matter* **12**, 1 (2015), arXiv:arXiv:1506.03501v1.
- [43] X. qing Shi, H. Chat, and Y. qiang Ma, *New J. Phys.* **16**, 035003 (2014).

- [44] J. V. Selinger and R. F. Bruinsma, *Phys. Rev. A* **43**, 2910 (1991).
- [45] M. Dijkstra and D. Frenkel, *Phys. Rev. E* **51**, 5891 (1995).
- [46] A. A. Joshi, J. K. Whitmer, O. Guzmán, N. L. Abbott, and J. J. de Pablo, *Soft Matter* **10**, 882 (2014).
- [47] Note that this 2D system with soft-core interactions should exhibit quasi-long-range order in the nematic phase [54–56], and thus  $S$  decays with system size. Since we are interested in the degree of order on the scale of typical bend and splay fluctuations, we report  $S$  values measured within regions of size  $10 \times 10\sigma^2$  (see [36]).
- [48] S. Mishra and S. Ramaswamy, *Phys. Rev. Lett.* **97**, 090602 (2006).
- [49] S. Ngo, A. Peshkov, I. S. Aranson, E. Bertin, F. Ginelli, and H. Chaté, *Phys. Rev. Lett.* **113**, 038302 (2014), arXiv:1312.1076.
- [50] E. Putzig and A. Baskaran, *Phys. Rev. E* **90**, 042304 (2014), 1057984.
- [51] S. Ramaswamy, R. A. Simha, and J. Toner, *Europhys. Lett.* **62**, 196 (2003).
- [52] H. Chaté, F. Ginelli, and R. Montagne, *Phys. Rev. Lett.* **96**, 180602 (2006).
- [53] H. P. Zhang, A. Be'er, E.-L. Florin, and H. L. Swinney, *Proc. Natl. Acad. Sci. U. S. A.* **107**, 13626 (2010), <http://www.pnas.org/content/107/31/13626.full.pdf>.
- [54] J. P. Straley, *Phys. Rev. A* **4**, 675 (1971).
- [55] D. Frenkel and R. Eppenga, *Phys. Rev. A* **31**, 1776 (1985).
- [56] J. M. Kosterlitz and D. J. Thouless, *J. Phys. C: Solid State Phys.* **6**, 1181 (1973).

# Supplementary material: The interplay of activity and filament flexibility determines the emergent properties of active nematics

Abhijeet Joshi, Elias Putzig, Aparna Baskaran, and Michael F. Hagan  
*Martin Fisher school of physics, Brandeis University, Waltham, MA 02453, USA*  
 (Dated: September 5, 2018)

## CONTENTS

S1. Simulation movies	1
S2. Model and simulation details	1
S3. Additional figures on scaling of active nematic characteristics with $\kappa_{\text{eff}}$	3
S4. Estimating the individual filament persistence length	3
S5. Splay and bend deformations	5
S6. Testing the scaling form for the effective bending rigidity	8
S7. System size effects	9
S8. Density fluctuations	9
S9. Defect identification and shape measurement algorithm	10
References	12

## S1. SIMULATION MOVIES

Animations of simulation trajectories (showing 1/16 of the simulation box) are provided for the following parameter sets, with  $k_b = 300$  and  $\tau_1 = 0.2$  in all cases:

- fa5\_k500\_t0p2.mp4:  $\kappa_{\text{eff}} = 20 : \kappa = 500, f^a = 5$
- fa5\_k2500\_t0p2.mp4:  $\kappa_{\text{eff}} = 100 : \kappa = 2500, f^a = 5$
- fa10\_k200\_t0p2.mp4:  $\kappa_{\text{eff}} = 2 : \kappa = 200, f^a = 10$
- fa10\_k2500\_t0p2.mp4:  $\kappa_{\text{eff}} = 25 : \kappa = 2500, f^a = 10$
- fa30\_k10000\_t0p2.mp4:  $\kappa_{\text{eff}} = 11 : \kappa = 10^4, f^a = 30$

In the videos, white arrows indicate positions and orientations of  $+\frac{1}{2}$  defects and white dots indicate positions of  $-\frac{1}{2}$  defects. Filament beads are colored according to the orientations of the local tangent vector.

## S2. MODEL AND SIMULATION DETAILS

*Interaction potentials:* We simulate the dynamics for the system of active filaments according to the following Langevin equation for each filament  $\alpha$  and bead  $i$  (with filaments indexed by Greek letters,  $\alpha = 1 \dots N$ , and beads within a filament indexed in Roman,  $i = 1 \dots M$ )

$$m\ddot{\mathbf{r}}_{\alpha,i} = \mathbf{f}_{\alpha,i}^a - \gamma\dot{\mathbf{r}}_{\alpha,i} - \nabla_{\mathbf{r}_{\alpha,i}}U + \mathbf{R}_{\alpha,i}(t). \quad (\text{S1})$$

with  $m$  as the bead mass,  $\mathbf{r}_{\alpha,i}$  as the bead position,  $f^a$  as the active force,  $U$  as the interaction potential which gives rise to the conservative forces,  $\gamma$  as the friction coefficient providing the damping and  $\mathbf{R}_{\alpha,i}(t)$  as a delta-correlated thermal noise with zero mean and variance  $\langle \mathbf{R}_{\alpha,i}(t) \cdot \mathbf{R}_{\beta,j}(t') \rangle = 4\gamma k_B T \delta_{\alpha,\beta} \delta_{i,j} \delta(t-t')$ .

The interaction potential includes three contributions which respectively account for non-bonded interactions between all bead pairs, stretching of each bond, and the angle potential between each pair of neighboring bonds:

$$\begin{aligned}
U(\{\mathbf{r}_{\alpha,i}\}) = & \frac{1}{2} \sum_{\alpha,\beta=1}^N \sum_{i,j=1}^M (1 - \delta_{\alpha,\beta} \delta_{i,j}) U_{\text{nb}}(|\mathbf{r}_{\beta,j} - \mathbf{r}_{\alpha,i}|) \\
& + \sum_{\alpha=1}^N \sum_{i=2}^M U_{\text{s}}(|\mathbf{r}_{\alpha,i} - \mathbf{r}_{\alpha,i-1}|) \\
& + \sum_{\alpha=1}^N \sum_{i=3}^M U_{\text{angle}}(\theta_{\alpha,i,i-1,i-2})
\end{aligned} \tag{S2}$$

with  $\theta_{\alpha,i,j,k}$  the angle made by the bead triplet  $\{i,j,k\}$  on filament  $\alpha$ . The non-bonded interactions account for steric repulsion and are modeled with the Weeks-Chandler-Anderson potential[1]

$$U_{\text{nb}}(r) = 4\varepsilon \left( (\sigma/r)^{12} - (\sigma/r)^6 + 1/4 \right) \Theta(2^{1/6}\sigma - r) \tag{S3}$$

with  $\varepsilon$  controlling the strength of steric repulsion and  $\Theta(x)$  the Heaviside function specifying the cutoff. Bond stretching is controlled by a FENE potential [2]

$$U_{\text{s}}(r) = -1/2k_{\text{b}}R_0^2 \ln \left( 1 - (r/R_0)^2 \right) \tag{S4}$$

with bond strength  $k_{\text{b}}$  and maximum bond length  $R_0$ . The angle potential is given by

$$U_{\text{angle}}(\theta) = \kappa (\theta - \pi)^2 \tag{S5}$$

where  $\kappa$  is the filament bending modulus.

Finally, activity is modeled as a propulsive force on every bead directed along the filament tangent toward its head. To render the activity nematic, the head and tail of each filament are switched at stochastic intervals so that the force direction on each bead rotates by 180 degrees. In particular, the active force has the form,  $\mathbf{f}_{\alpha,i}^a(t) = \eta_{\alpha}(t) f^a \mathbf{t}_{\alpha,i}$ , where  $f^a$  parameterizes the activity strength, and  $\eta_{\alpha}(t)$  is a stochastic variable associated with filament  $\alpha$  that changes its values between 1 and  $-1$  on Poisson distributed intervals with mean  $\tau_1$ , so that  $\tau_1$  controls the reversal frequency. The local tangent vector  $\mathbf{t}_{\alpha,i}$  along the filament contour at a bead  $i$  is calculated as

$$\mathbf{t}_{\alpha,i} = \begin{cases} \frac{\mathbf{r}_{\alpha,i+1} - \mathbf{r}_{\alpha,i-1}}{|\mathbf{r}_{\alpha,i+1} - \mathbf{r}_{\alpha,i-1}|}, & \text{for } i = 2, \dots, M-1 \\ \frac{\mathbf{r}_{\alpha,2} - \mathbf{r}_{\alpha,1}}{|\mathbf{r}_{\alpha,2} - \mathbf{r}_{\alpha,1}|}, & \text{for } i = 1 \\ \frac{\mathbf{r}_{\alpha,M} - \mathbf{r}_{\alpha,M-1}}{|\mathbf{r}_{\alpha,M} - \mathbf{r}_{\alpha,M-1}|} & \text{for } i = M. \end{cases}$$

*Simulations and parameter values:* We set mass of the each bead to  $m = 1$  and the damping coefficient to  $\gamma = 2$ . With these parameters inertia is non-negligible. In the future, we plan to systematically investigate the effect of damping. We report lengths and energies in units of the bead diameter  $\sigma = 1$  and the thermal energy at a reference state,  $k_B T_{\text{ref}}$ . Time is measured in units of  $\tau = \sqrt{m\sigma^2/k_B T_{\text{ref}}}$ . Eqs. (S1) were integrated with time step  $\delta t = 10^{-3}\tau$  using LAMMPS [3], with an in-house modification to include the active propulsion force. We set the repulsion parameter  $\varepsilon = k_B T_{\text{ref}}$  (the results are insensitive to the value of  $\varepsilon$  provided it is sufficiently high to avoid filament overlap). We performed simulations in a  $A = 840 \times 840\sigma^2$  periodic simulation box, with  $N = 19404$  filaments each with  $M = 20$  beads, so that the packing fraction  $\phi = MN\sigma^2/A \approx 0.55$ .

In the FENE bond potential,  $R_0$  is set to  $1.5\sigma$  and  $k_{\text{b}} = 300k_B T_{\text{ref}}/\sigma^2$  for the simulations in the main text (see next paragraph). The temperature is set to  $T = 3.0k_B T_{\text{ref}}$ . These parameters lead to a mean bond length of  $b \approx 0.84\sigma$ , which ensures that filaments are non-penetrable for the parameter space explored in this work. Finally,  $L = (M-1)b$  is the mean filament length. In semiflexible limit, the stiffness  $\kappa$  in the discrete model is related to the continuum bending modulus  $\tilde{\kappa}$  as  $\kappa \approx \tilde{\kappa}/2b$ , and thus the persistence length is given by  $l_p = 2b\kappa/k_B T$ .

We performed two sets of simulations. Initially, we set the FENE bond strength  $k_{\text{b}} = 30k_B T_{\text{ref}}/\sigma^2$  and  $\tau_1 = \tau$ , thus maintaining the reversal frequency of active propulsion to a fixed value while varying filament stiffness,  $\kappa \in [100, 2500]k_B T_{\text{ref}}$  and the magnitude of the active force. However, for these parameters we discovered that interpenetration of filaments becomes possible at large propulsion velocities, thus limiting the simulations to  $f^a \leq 10$ .



To enable investigating higher activity values, we therefore performed a second set of simulations (those reported in the main text) with higher FENE bond strength,  $k_b = 300k_B T_{\text{ref}}/\sigma^2$  and shorter reversal timescale  $\tau_1 = 0.2$ , with  $\kappa \in [100, 10000]k_B T_{\text{ref}}$ . This enables simulating activity values up to  $f^a \leq 30$ .

The shorter reversal timescale was needed in the new set of simulations because when the product  $f^a \tau$  exceeds a characteristic collision length scale the self-propulsion becomes polar in nature and model is no longer a good description of an active nematic. In particular, the filaments behave as polar self-propelled rods, as evidenced by the formation of polar clusters [4–8]. Interestingly, increasing  $k_b$  increases the rate of defect formation and decreases the threshold value of  $f^a \tau$  above which phase separation occurs. We monitored the existence of phase separation by measuring local densities within simulation boxes (see below). We found no significant phase separation (except on short scales, see below) or formation of polar clusters for any of the simulations described here, indicating the systems were in the nematic regime. Within the nematic regime, increasing  $k_b$  does not qualitatively change results or scaling relations, although it does quantitatively shift properties such as the defect density. The scaling of defect density with  $\kappa$  and  $f^a$  for the simulations with  $k_b = 30$  is shown in Fig. S1.

In our simulations we have fixed the filament length at  $M = 20$  beads. Exploratory simulations showed that varying  $M$  does not change the scaling of observables with  $\kappa_{\text{eff}}$ , although it shifts properties such as the defect density since the total active force per filament goes as  $f^a M$ . The maximum persistence length above which scaling laws fail is also proportional to filament length:  $\kappa_{\text{eff}}^{\text{max}} = k_B T M / 2b$

*Initialization:* We initialized the system by first placing the filaments in completely extended configurations (all bonds parallel and all bond lengths set to  $b$ ), on a rectangular lattice aligned with the simulation box, with filaments oriented along one of the lattice vectors. We then allowed this initial configuration to relax by simulating for  $10^4 \tau$ , before performing production runs of  $\sim 4 \times 10^4 \tau$ . As noted in the main text, the equilibration time of  $10^4 \tau$  was chosen based on the fact that in all simulated systems the defect density had reached steady state by this time. We also confirmed that other observables of interest have reached steady state at this time. In the limit of high stiffness or low activity, we found that defect nucleation from the unphysically crystalline initial condition did not occur on computationally accessible timescales, thus prohibiting relaxation. In these cases, we used an alternative initial configuration, with filaments arranged into four rectangular lattices, each placed in one quadrant of the simulation box such that adjacent (non-diagonal) lattices are orthogonal.

*Analysis:* To analyze our simulation trajectories within the framework of liquid crystal theory, we calculated the local nematic tensor as  $Q_{\alpha\beta}(r_{ij}) = \sum_{k, |r_k - r_{ij}| < 5\sigma} (t_{k\alpha} t_{k\beta} - \frac{1}{2} \delta_{\alpha\beta})$  and the density field  $\rho$  on a  $1000 \times 1000$  grid, where,  $r_{ij}$  is the position of the grid point and  $r_k$  and  $t_k$  are the positions and tangent vectors of all segments. We then evaluated the local nematic order parameter,  $S$  and director  $\hat{n}$  as the largest eigenvalue of  $Q$  and corresponding eigenvector. We identified defects in the director field and their topological charges using the procedure described in section S9 below. To compare the magnitudes of splay and bend deformations in our active systems to those that occur at equilibrium, we calculated elastic constants of our system at equilibrium ( $f^a = 0$ ) using the free energy perturbation technique proposed by Joshi et al. [9]. We performed these equilibrium calculations on a box of size  $64 \times 64 \sigma^2$ .

### S3. ADDITIONAL FIGURES ON SCALING OF ACTIVE NEMATIC CHARACTERISTICS WITH $\kappa_{\text{eff}}$

We present data on defect density from the alternative data set described in section S2 in Fig. S1, and an explicit listing of parameter values for Fig. 3 in the main text in Fig. S2.

### S4. ESTIMATING THE INDIVIDUAL FILAMENT PERSISTENCE LENGTH

In this section we describe estimates of the effective persistence length measured from the tangent fluctuations of individual filaments. We performed these measurements both on individual filaments within a bulk active nematic, and isolated individual filaments to distinguish single-chain and multi-chain effects on the effective persistence length.

In a continuum limit, the total bending energy of a semiflexible filament it is well approximated by the wormlike chain model [10],

$$H_{\text{bend}} = \frac{\tilde{\kappa}}{2} \int_0^L \left( \frac{d\theta}{ds} \right)^2 ds \quad (\text{S6})$$

where the integration is over the filament contour length,  $L$ , parameterized by  $s$ ,  $\tilde{\kappa}$  is the continuum bending modulus, and  $\theta(s)$  is the tangent angle along the contour.

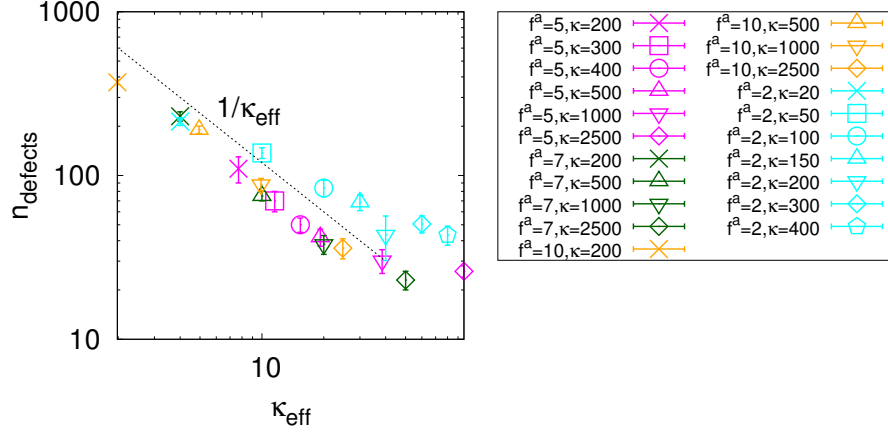


FIG. S1. Number of defects as a function of  $\kappa_{\text{eff}}$  for the alternative dataset, with FENE bond strength  $k_b = 30$  and active reversal period,  $\tau_1 = 1$ . Notice that we observe data collapse for all parameters with  $f^a \geq 5$ , but not for the lowest activity  $f^a = 2$  (light blue symbols), when the system begins to lose nematic order (see Fig. S7c below) and the active force strength becomes comparable to thermal forces.

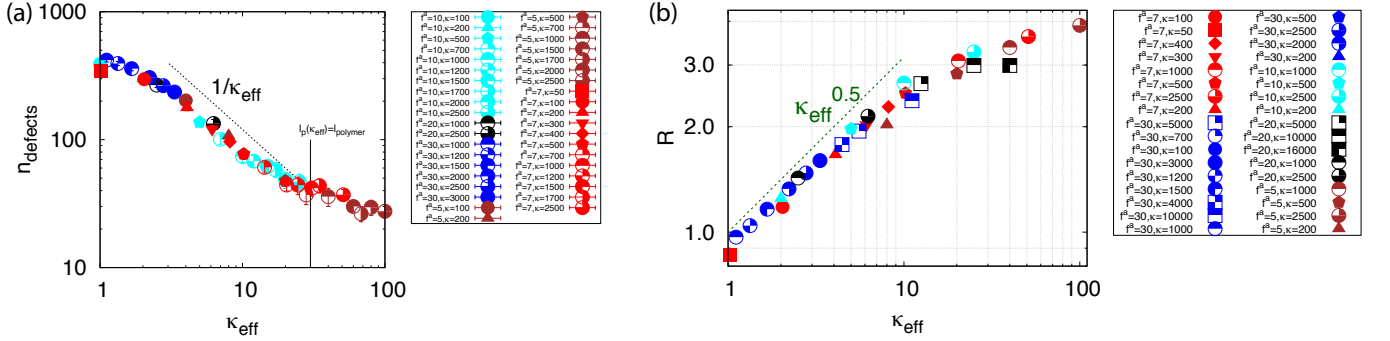


FIG. S2. Specification of all data points considered for the main data set ( $k_b = 300$  and  $\tau_1 = 0.2$ ) (a) Defect density as a function of  $\kappa_{\text{eff}}$  for indicated values of  $f^a$  and  $\kappa$ . (b) Ratio of splay/bend ( $R$ , defined in the main text) as a function of  $\kappa_{\text{eff}}$  for indicated values of  $f^a$  and  $\kappa$ .

For a normal-mode analysis of the bending excitations we performed a Fourier decomposition of the tangential angle  $\theta(s)$  assuming general boundary conditions (since a filament in bulk need not be force-free at its ends):

$$\theta(s) = \sum_q (a_q \cos(qs) + b_q \sin(qs)) \quad (\text{S7})$$

where  $q = n\pi/L$  ( $n = 1, 2, 3, \dots$ ) is the wave vector, with corresponding wavelength  $\lambda = \pi/q$ .

At equilibrium, using Eqs. (S6) and (S7) along with the equipartition theorem results in

$$\langle a_q^2 + b_q^2 \rangle = \frac{2k_B T}{\tilde{\kappa} L q^2}. \quad (\text{S8})$$

The modulus  $\tilde{\kappa}$  can then be estimated from the slope of  $\langle a_q^2 + b_q^2 \rangle$  vs.  $q$ , as shown for an example parameter set in Fig. S3b, and the persistence length is given by  $l_p = \tilde{\kappa}/k_B T$ .

Performing this procedure for our non-equilibrium system as a function of  $\kappa$  and  $f^a$  allows estimating the activity-renormalized filament persistence length. Fig. S3a shows estimated persistence lengths as a function of  $\kappa$  and  $f^a$  measured from individual chains from two sets of simulations: isolated chains (small solid symbols) and chains from the bulk active nematic (large open symbols). For chains within bulk, we observe data collapse when the effective persistence length is plotted as a function of  $\kappa_{\text{eff}}$  (provided  $f^a \geq 5$ ), with the same scaling found for the bulk bend modulus in the main text:  $l_p \sim \kappa_{\text{eff}}$ , consistent with the equilibrium result that the bulk bend modulus depends linearly on the filament modulus. In contrast, while the estimated persistence length scales linearly with  $\kappa$  for isolated chains,

we do not observe data collapse for isolated chains simulated at different activity strengths. This result supports the proposal in the main text that the observed scaling form for the activity-renormalized bend modulus arises due to inter-chain collisions. Furthermore, for  $f^a \geq 5$  the persistence length measured for isolated chains exceeds that of bulk chains, showing that the inter-chain collisions lead to an apparent softening of the filament modulus.

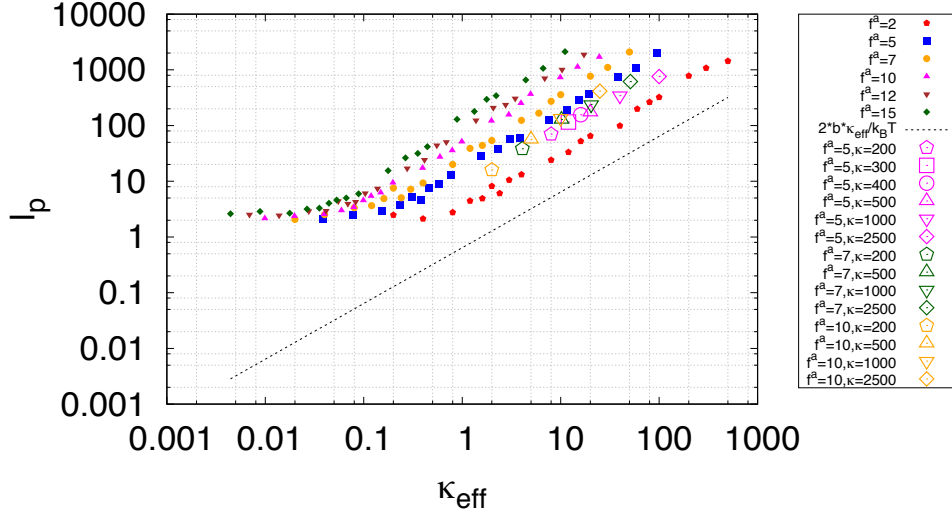


FIG. S3. Effective persistence length  $l_p$  estimated from the spectrum of filament tangent fluctuations in systems of isolated filaments (small filled symbols) and bulk active nematics (large open symbols). The dashed line has the slope of the expected scaling  $2b^*\kappa_{\text{eff}}/k_B T$ . We see that all results scale with the bare bending rigidity,  $l_p \sim \kappa$ , but only the results for the bulk systems exhibit data collapse for different activity strengths. The legend shows the value of  $\kappa$  and  $f^a$  for each system, and other parameters are  $\tau_1 = \tau$  and  $k_b = 30k_B T_{\text{ref}}/\sigma^2$ .

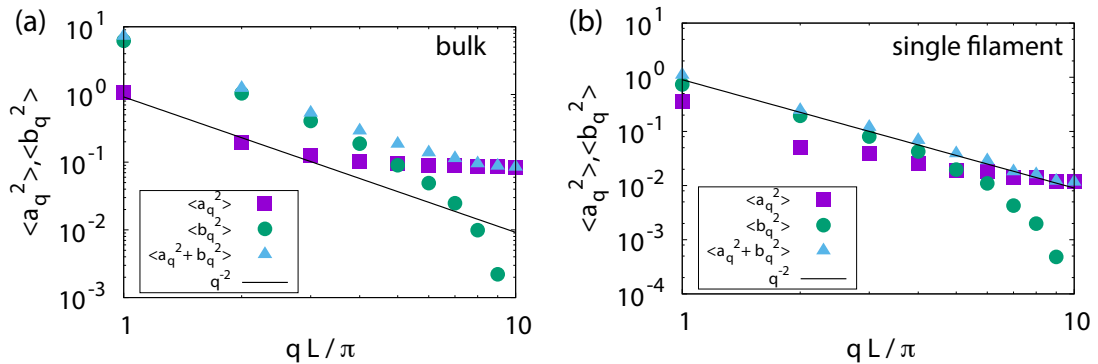


FIG. S4. Fourier amplitudes  $\langle a_q^2 \rangle$ ,  $\langle b_q^2 \rangle$  and  $\langle a_q^2 + b_q^2 \rangle$  as a function of wave vector  $qL/\pi$ , with  $L$  the box side length, measured in a simulation of (a) a bulk simulation and (b) an isolated filament, for representative parameter values ( $\kappa = 500, f^a = 10; \kappa_{\text{eff}} = 5$ ).

## S5. SPLAY AND BEND DEFORMATIONS

In a continuum description of a 2D nematic, all elastic deformations can be decomposed into bend and splay modes, given by  $\mathbf{d}_{\text{bend}}(\mathbf{r}) = \hat{n}(\mathbf{r}) \times (\nabla \times \hat{n}(\mathbf{r}))$  and  $d_{\text{splay}}(\mathbf{r}) = (\nabla \cdot \hat{n}(\mathbf{r}))$ . Fig. S5 shows the spatial distribution of bend and splay deformations in systems at low and high rigidity values. To avoid breakdown of these definitions within defect cores or other vacant regions, we have normalized the deformations by the local density and nematic

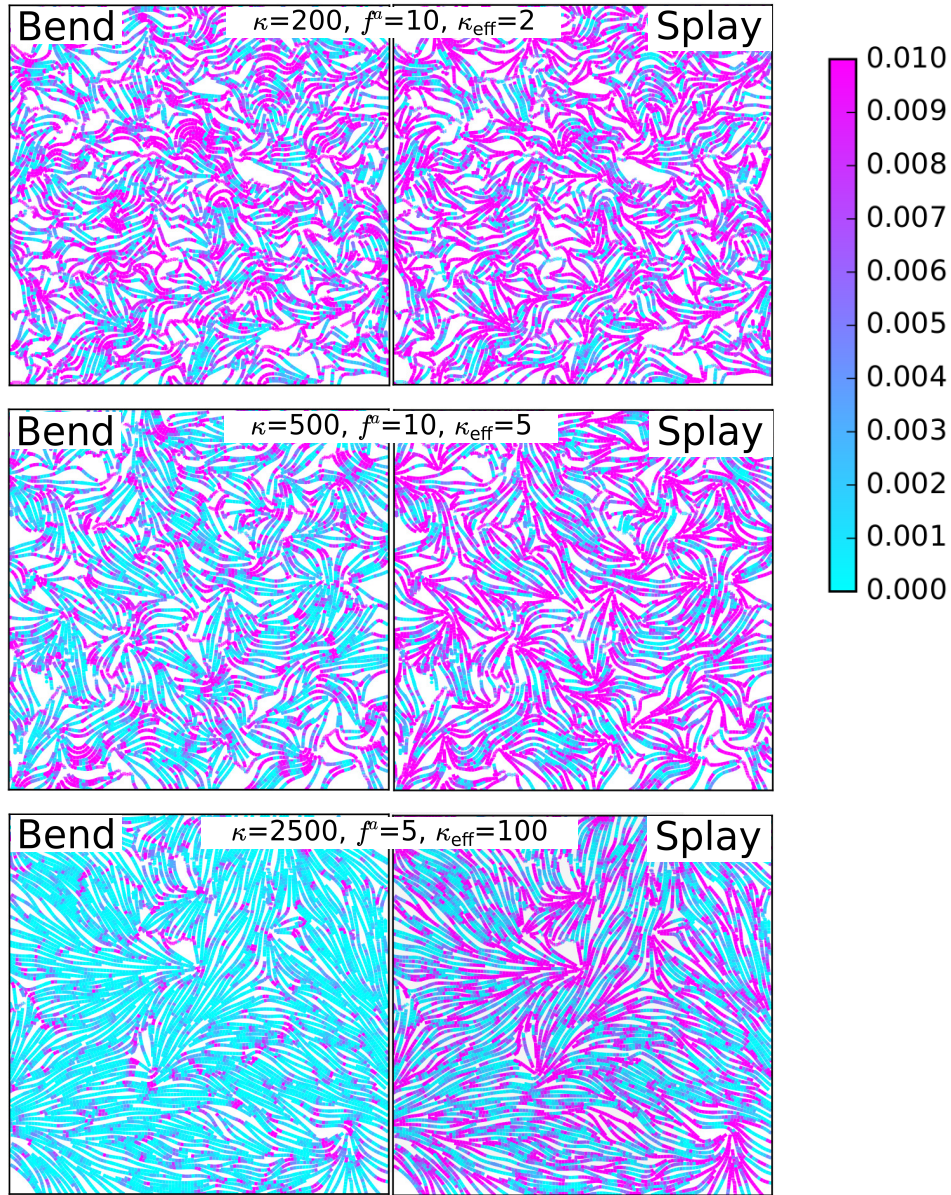


FIG. S5. Snapshots from steady state configurations at indicated parameter values, with colormaps showing the distribution of bend,  $\rho S^2(\hat{n} \times (\nabla \times \hat{n}))^2$  (left), and splay,  $\rho S^2(\nabla \cdot \hat{n})^2$  (right), superposed on lines representing the director field. The parameters are chosen to highlight differences between flexible (small  $\kappa_{\text{eff}}$ ) and rigid (large  $\kappa_{\text{eff}}$ ) systems. The color range is clipped at 0.01 to clarify the spatial variations of the deformations.

order:  $D_{\text{bend}} = \rho S^2 |\mathbf{d}_{\text{bend}}|^2$  and  $D_{\text{splay}} = \rho S^2 d_{\text{splay}}^2$ . We see that bend and splay are equally spread out in the system in the limit of low rigidity, whereas bend deformations are primarily located near defect cores for large rigidity. In the high rigidity simulations, the effective persistence length ( $\approx 66\sigma$ ) significantly exceeds the filament contour length ( $20\sigma$ ), and thus most bend deformations correspond to rotation of the director field around filament ends at a defect tip.

To obtain further insight into the spatial organization of deformations, we calculated power spectra as  $P_k^{\text{bend}} = \int d^2 \mathbf{r}' \exp(-i\mathbf{k} \cdot (\mathbf{r}')) \langle D_{\text{bend}}(\mathbf{r}) D_{\text{bend}}(\mathbf{r} + \mathbf{r}') \rangle$ , with an analogous definition for splay, and with the  $Q$  field calculated at  $1000 \times 1000$  grid points (a realspace gridspacing of  $0.84\sigma$ ). The resulting power spectra are shown in Fig. S6a,b as functions of the renormalized filament rigidity, and the dependences of the peak positions and maximal power are discussed in the main text. Here we note that the splay spectra exhibit asymptotic scaling of  $k^{5/3}$  and  $k^{-8/3}$  at scales respectively above the defect spacing or below the size of individual filaments, with a plateau region at intermediate scales. The same asymptotic scalings in power spectra were observed in dense bacterial suspensions in the turbulent

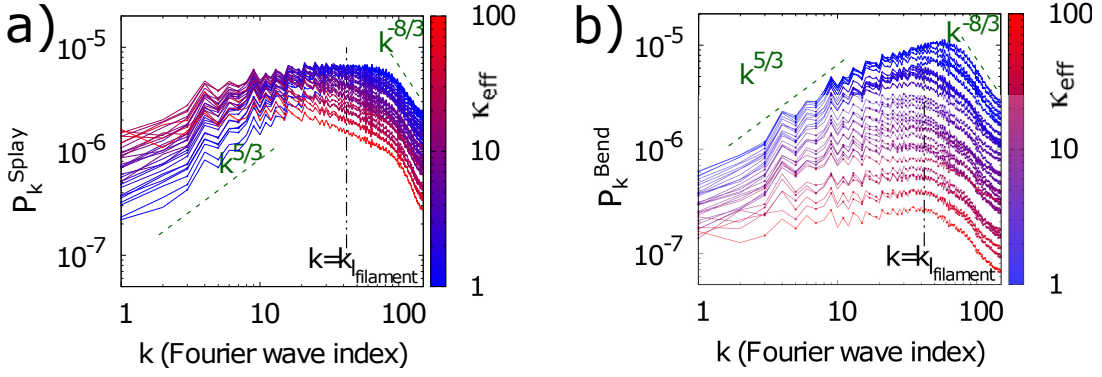


FIG. S6. Power spectrum of splay (a) and bend (b) deformations as a function of wavenumber  $k$ , with the colorbar indicating the value of effective bending rigidity ( $\kappa_{\text{eff}}$ ).

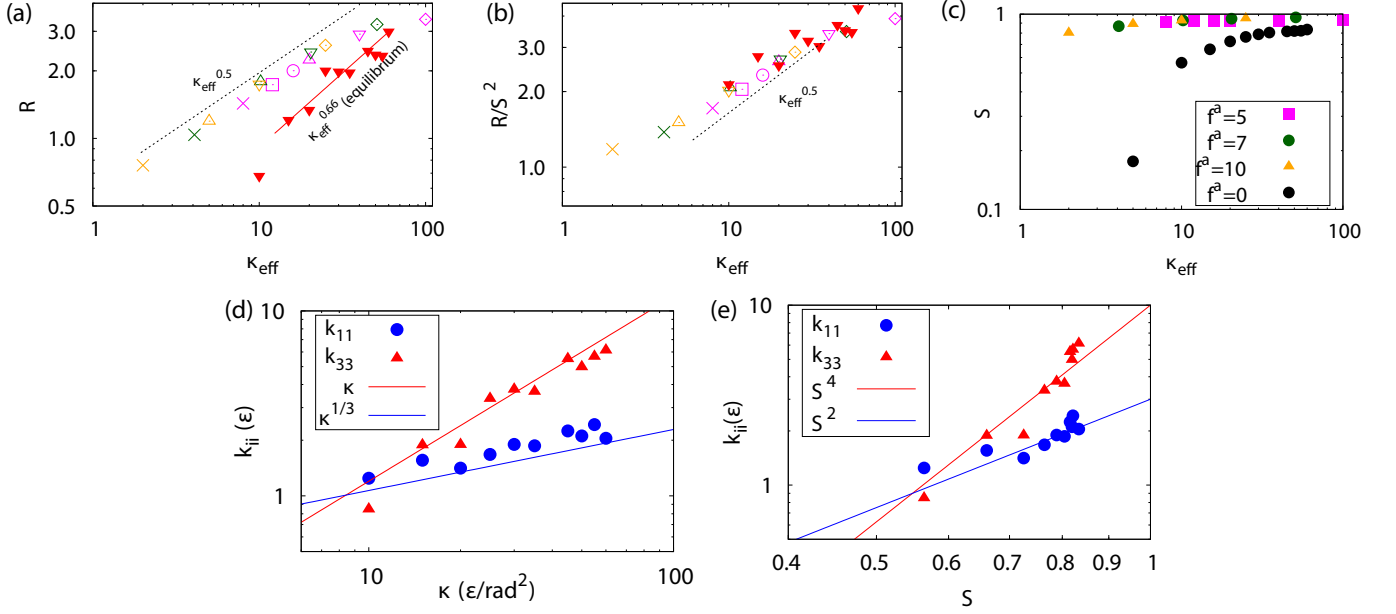


FIG. S7. Comparison of ratio of bend and splay deformations in an active nematic to an equilibrium system. (a) The ratio of splay and bend deformations,  $R$ , plotted as a function of renormalized bending rigidity for active and equilibrium systems. The ratio  $R$  calculated in equilibrium systems is shown as  $\blacktriangledown$  symbols, while the symbols for the active system are defined as in Fig. S1. (b) The data from (a) is shown normalized by the mean nematic order parameter squared,  $(R/S^2)$ . (c) The mean nematic order parameter,  $S$ , as a function of renormalized bending rigidity measured in active and equilibrium simulations. (d) Values of the bend ( $k_{33}$ ) and splay ( $k_{11}$ ) elastic constants as a function of  $\kappa$  calculated using free energy perturbation [9] in equilibrium simulations ( $f^a = 0$ ). (e) The same results as in (d), plotted against the nematic order parameter  $S$  calculated for each parameter value. The red and blue lines indicate scaling of  $\sim S^4$  and  $\sim S^2$ . The active results in this figure correspond to the additional data set with  $k_b = 30$  and  $\tau_1 = 1$ , as in Fig. S1.

regime [11, 12].

The main text discusses the ratio of total strain energy in splay deformations to those in bend

$$R = \left\langle \int d^2\mathbf{r} D_{\text{splay}}(\mathbf{r}) \right\rangle / \left\langle \int d^2\mathbf{r} D_{\text{bend}}(\mathbf{r}) \right\rangle. \quad (\text{S9})$$

We find that this ratio scales as  $R \sim \kappa_{\text{eff}}^{1/2}$  for all parameter sets, which is different from the expected scaling in an equilibrium nematic of  $R_{\text{eq}} \sim \kappa^{2/3}$ . To investigate the origins of this discrepancy, we measured the elastic moduli for an equilibrium system for different  $\kappa$  values shown in Fig. (S7). We find that the degree of order in the system depends on the value of  $\kappa$ , that approximate scalings can be identified as  $k_{33} \sim S^4$  and  $k_{11} \sim S^2$  (Fig. (S7b)), and that the amount of order in the system at a given stiffness value  $\kappa_{\text{eff}}$  is very different for active nematics when compared



to their equilibrium analogs (Fig. (S7c)). Active nematics have considerably higher order, possibly because their intrinsic tendency to phase separate [13, 14] leads to higher local density in comparison to an equilibrium system at corresponding  $\rho$  and  $\kappa_{\text{eff}}$ . We used this information to empirically find that  $R/S^2$  exhibits approximately the same scaling for active and passive nematics.

Finally, by analogy to equipartition at equilibrium, the ratio of splay/bend,  $R$ , can be construed as an effective ratio of moduli:  $k_{33}^{\text{effective}}/k_{11}^{\text{effective}}$ , with the ratio depending on activity. Fig. S8 shows the defect shape parameter plotted as a function of this ratio.

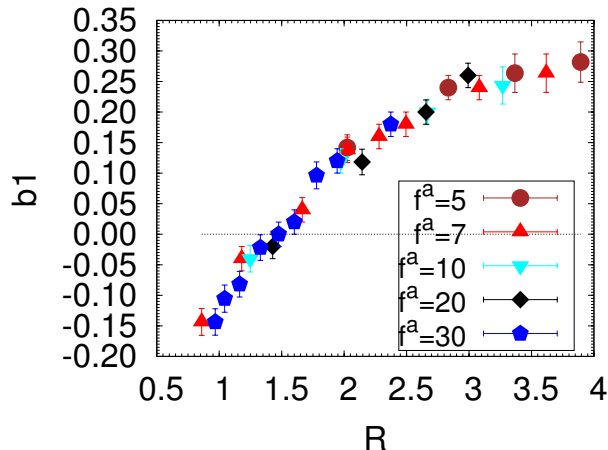


FIG. S8. Defect shape parameter  $b_1$  as a function of splay/bend ratio  $R$  defined in the text, for the data in Fig. 3b,c of the main text.

## S6. TESTING THE SCALING FORM FOR THE EFFECTIVE BENDING RIGIDITY

Fig. S9 shows two alternative scaling forms for the activity-renormalized bending rigidity  $\kappa_{\text{eff}}$ , with data from a wide range of activity values ( $(f^a)^2 \in [25, 900]$ ). We see that only the form presented in the main text,  $\kappa_{\text{eff}} \cong \kappa/f^{a^2}$  (Fig. 3 main text) leads to data collapse from simulations with different activity levels.

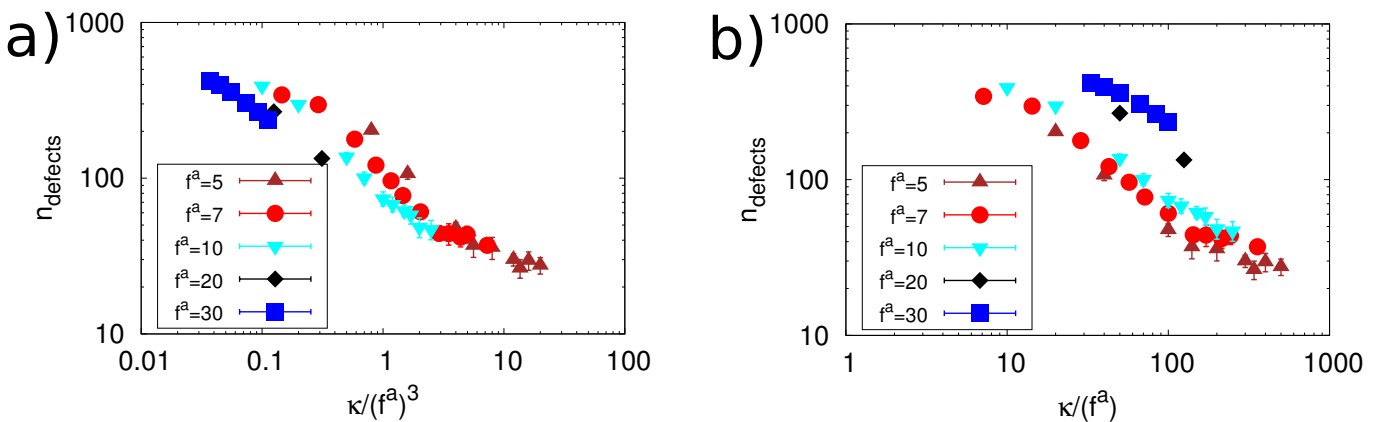


FIG. S9. The data from Fig. 3 (main text) for defect densities measured in simulations at varying  $\kappa$  and  $f^a$  is plotted according to two alternative scaling forms for the activity-renormalized bending rigidity: (a)  $\kappa_{\text{eff}} = \kappa/(f^a)^3$  and (b)  $\kappa_{\text{eff}} = \kappa/f^a$ .



## S7. SYSTEM SIZE EFFECTS

To assess finite size effects on our results, we performed a system size analysis for two parameter sets from Fig. S1:  $\kappa = 200$ ,  $f^a = 5$  and  $\kappa = 2500$ ,  $f^a = 5$ , with  $\tau_1 = \tau$  and  $k_b = 30$ . We chose these parameter sets because they are near the upper and lower limits of effective bending rigidity investigated in that set of simulations. As shown in Fig. S10, we observe no systematic dependence of defect density on system size over the range of side lengths  $L \in [200, 1200]\sigma$ . We observe a similar lack of dependence on system size for other observables, suggesting that finite size effects are negligible in our simulations at system size ( $840 \times 840\sigma^2$ ).

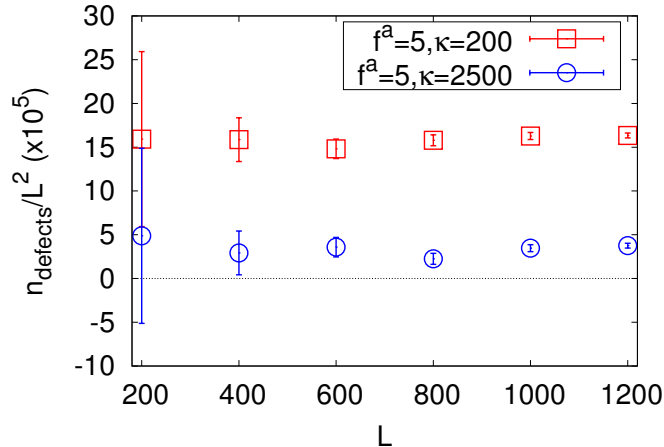


FIG. S10. Steady-state defect density as a function of simulation box side length  $L$  for square boxes with periodic boundary conditions, at indicated values of the filament modulus and activity parameter, with  $\tau_1 = \tau$  and  $k_b = 30k_B T_{\text{ref}}$ .

## S8. DENSITY FLUCTUATIONS

It is well-known that active nematics are susceptible to phase separation [13, 15–17] and giant number fluctuations (GNFs) [13, 14, 18–20]. We therefore monitored these quantities in our system. Interestingly, while we do observe large density fluctuations on small scales (see videos of typical trajectories), phase separation is suppressed on large scales in the semiflexible regime. Fig. S11 shows histograms of local density, measured within subsystems with side length  $10\sigma$  as a function of  $\kappa$ . We see that the distribution of local densities broadens as  $f^a$  and  $\kappa$  increase, but remains unimodal indicating an absence of true phase separation.

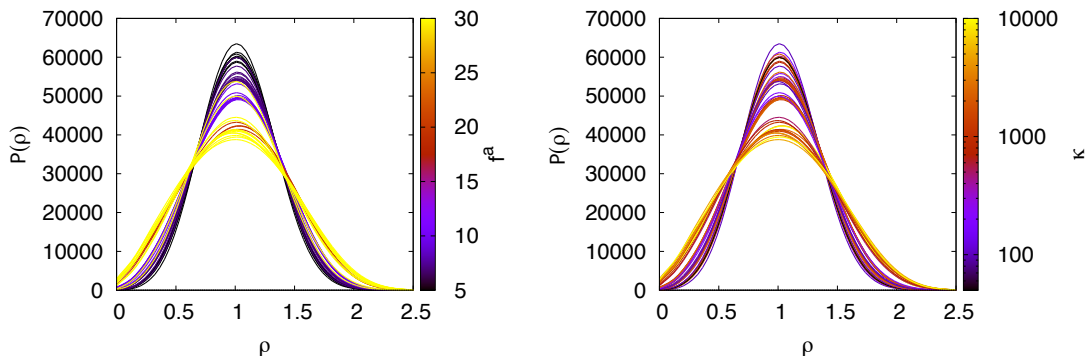


FIG. S11. The distribution of local densities of filament pseudoatoms for indicated values of activity (**left**) and bare bending rigidity (**right**). Local densities were calculated by measuring the number of filament beads within square subsystems with side length  $10\sigma$ .

We also monitored the existence of GNFs, by measuring the number of pseudoatoms within square subsystems with

side lengths ranging from  $20\sigma$  to  $840\sigma$  as a function of time. At equilibrium, in a region containing on average  $N$  particles the standard deviation of the number of particles  $\Delta N$  scales as  $\Delta N \sim \sqrt{N}$ , while previous studies of active nematics have identified higher scaling, as large as  $\Delta N \sim N$ . Consistent with the other characteristics of an active nematic studied in this article, we find that the scaling of number fluctuations depends only on the effective bending modulus  $\kappa_{\text{eff}}$ . Fig. S12a shows measured number fluctuations for different values of the effective bending modulus, plotted as  $\Delta N/\sqrt{N}$ , so that the result will be constant with subsystem size for a system exhibiting equilibrium-like fluctuations. We see that for small  $\kappa_{\text{eff}} = 2$  the result is constant with subsystem size, indicating equilibrium-like fluctuations, but the slope increases for  $\kappa_{\text{eff}} = 10$  and  $\kappa_{\text{eff}} = 100$  indicating a progression toward GNFs. At all  $\kappa_{\text{eff}}$  the fluctuations are eventually suppressed on scales comparable to the defect spacing ( $N \gtrsim 10^4$ ), at which scale the system is essentially isotropic, consistent with Narayan et al. [19].

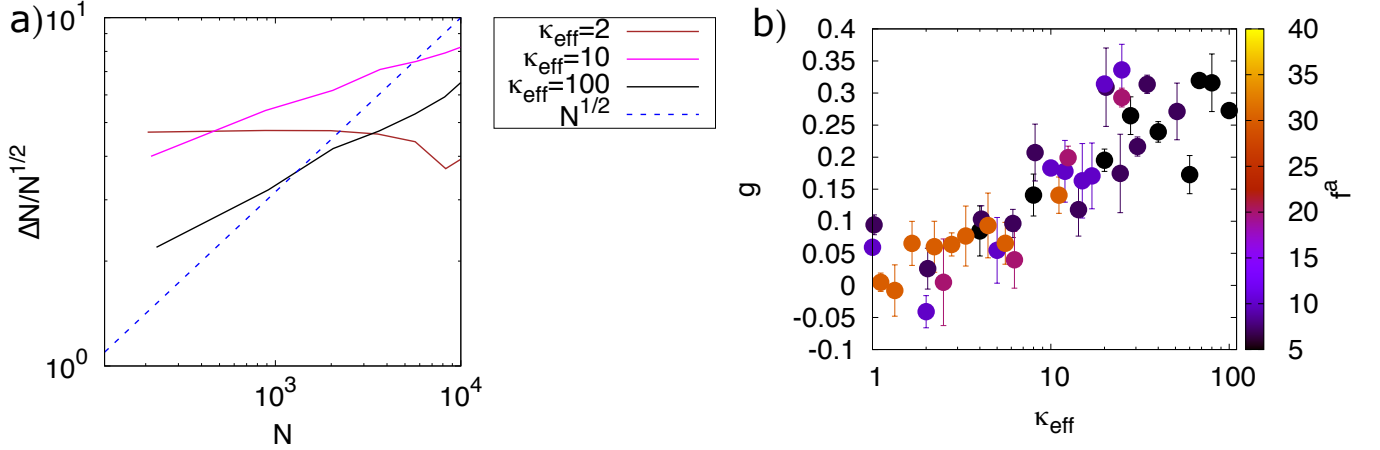


FIG. S12. Giant number fluctuations (GNFs) depend on the renormalized bending rigidity. (a). The mean fluctuations of number of filament pseudoatoms,  $\Delta N$ , is plotted as a function of subsystem size  $N$  for representative values of  $\kappa_{\text{eff}}$ . The fluctuations are normalized by their value at equilibrium,  $\Delta N/\sqrt{N}$  so that a horizontal line indicates equilibrium-like fluctuations. (b) The fluctuation scaling exponent  $g$  is plotted as a function of  $\kappa_{\text{eff}}$ . We determined  $g$  by fitting the dependence of fluctuations on subsystem size for each parameter set to the form  $\Delta N/\sqrt{N} = aN^g$  over the range  $N \leq 10^4$ . Note that a value of  $g = 0$  corresponds to equilibrium-like fluctuations, while  $g = 0.5$  would correspond to  $\Delta N \sim N$ .

To determine the dependence on  $\kappa_{\text{eff}}$ , we fit the data for each simulation in the range  $N \leq 10^4$  to the form  $aN^g$ , so that  $g = 0$  indicates equilibrium-like fluctuations and  $g = 0.5$  would indicate linear scaling of fluctuations with system size. As shown in Fig. S12b,  $g$  increases with  $\kappa_{\text{eff}}$ , with  $g = 0$  for small  $\kappa_{\text{eff}}$  and  $g \approx 0.3$  for the largest renormalized bending rigidity values investigated; *i.e.*  $\Delta N \sim N^{0.8}$ . The fact that  $g < 0.5$  for the parameters we consider may reflect suppression of fluctuations even for  $N < 10^4$ . Importantly, estimated values of  $g$  at different  $f^a$  and  $\kappa$  collapse onto a single function of  $\kappa_{\text{eff}}$ , consistent with the observations of other characteristics (Fig. 3 in the main text). We speculate that we do not observe GNFs for small renormalized bending rigidity values because GNFs are suppressed on scales beyond the defect spacing.

## S9. DEFECT IDENTIFICATION AND SHAPE MEASUREMENT ALGORITHM

Here, we provide details on how we identify and measure the shapes of defects from our simulation data. This algorithm can also be directly applied to retardance images from experimental systems, and discretized output from continuum simulations.

Locating and identifying defects: We locate defects using the fact the magnitude of nematic order  $S$  is very small at defect cores. We first compute the magnitude  $S = 2\sqrt{Q_{xx}^2 + Q_{xy}^2}$  from the nematic tensor, whose measurement was described above. The regions corresponding to defect cores can then be extracted by using a flood-fill algorithm to select connected areas where the order is below some threshold  $S_{\text{threshold}}$ . We set  $S_{\text{threshold}} = 0.6$  since the system is deep within the nematic state for the parameters of this study. Once the defect cores have been located, the charge of each defect can be identified from the total change in the orientation of the director in a loop around the defect core. We perform this calculation by adding the change in angle for points in a circle about the center of the core. We choose the radius of the circle to be at least  $5\sigma$ , to ensure a well defined director field. The total change in angle must be a multiple of  $\pi$ :  $\Delta\theta = n\pi$ , where if  $n = 0$  then the disordered region is not a defect, and otherwise it is a

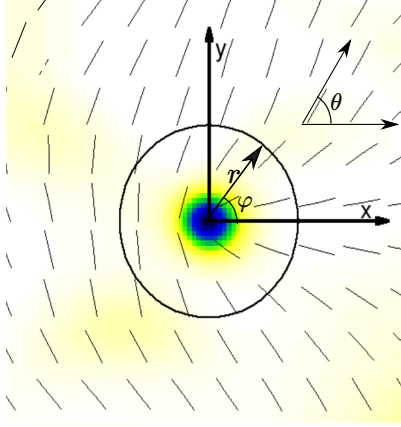


FIG. S13. Schematic showing the defect-centered coordinate system defined in the text, with azimuthal angle  $\phi$  and director angle  $\theta(r, \phi)$ . Note that the  $x$ -axis is chosen along the orientation vector of the  $+1/2$  defect given by the angle  $\theta'_0$  defined in the text.

defect with topological charge  $m = \frac{n}{2}$ . Typically  $n = \pm 1$  but, in rare cases we observed defects with charge  $m = +1$  in our simulation data.

Identifying the orientations and characterizing the shapes of  $+1/2$  defects: Given the location of a defect and its charge, there are several methods which can be used to measure the orientation of the  $+1/2$  defects [21, 22]. In this work, we compute the sum of the divergence of  $\mathbf{Q}$  field,  $\nabla_\beta Q_{\alpha\beta}$  along a circle enclosing the defect, and normalize it to a give unit vector. This unit vector represents the orientation of the  $+1/2$  defect and in our two dimensional system identifies an angle  $\theta'_0$  for the defect.

We then measure the director orientation  $\bar{\theta}(\bar{\phi})$  along the azimuthal angle  $\bar{\phi}$  at discrete set of radii,  $\{r\}$ , around the defect core. First, we ensure that each loop does not cross any disordered regions, or enclose any other defects, by checking the order at each point and summing  $\Delta\theta$  over the loop. Then we apply a coordinate frame rotation such that  $\theta = \bar{\theta} - \theta'_0$ , and the azimuthal angle  $\phi = \bar{\phi} - \theta'_0$ , where,  $\theta'_0$  is an orientation of the  $+1/2$  defect estimated above. This step rotates the coordinate frame of reference to the frame of reference of the  $+1/2$  defect. Finally, we evaluate the Fourier coefficients for  $\theta(\phi)$ ,

$$\theta(r, \phi) = +\frac{1}{2}\phi + \sum_n a_n(r) \cos(n\phi) + b_n(r) \sin(n\phi). \quad (\text{S10})$$

However, in practice we find that truncating the expansion after the first sin term gives an excellent approximation of the shape of a  $+1/2$  defect. Hence, once a value of  $r$  is chosen, the defect can be characterized by the single parameter  $b_1$ .

In Fig. S14 we show the distribution of  $b_1$  values obtained from our simulations with  $r = 12.6\sigma$ . Note that we observe long tailed distributions of  $b_1$  with tails in the  $b_1 < 0$  regime. However, the distributions are sharply peaked with typical peak width  $\sim 0.1$ . Therefore we consider the mode of  $b_1$  values as an appropriate measure of defect shape.

Choice of  $r$ : For an isolated defect,  $b_1$  asymptotes once the distance from the defect center increases beyond the core size. However, as noted in Zhou et al. [23], in a system with finite defect density the defect shape should be parameterized as close to the defect center as possible to avoid distortion due to other defects. The typical defect core radius in our simulations (defined as the region in which the nematic order parameter  $S < 0.6$ ) is about  $4\sigma$ . The smallest defect spacing (at the highest defect density) in our simulations is about  $40\sigma$ . We therefore chose a radius  $r = 12.6\sigma$ , where the nematic is highly ordered and the director is always well-defined, but distortions due to other defects are minimized. As shown in Fig. S14b the results are qualitatively insensitive to radius for  $r > 5$ , although statistics become more limited for larger  $r$ . For consistency, the same radius should be chosen for all systems.

Breakdown at high  $f^a$  and  $\kappa$ : As noted in the main text, the defect identification algorithm breaks down in systems with both extremely high activity and high bare bending rigidity ( $f^a \geq 20$  and  $\kappa \gtrsim 5000$ ). Under these conditions the system exhibits density fluctuations on very short length scales (see Fig. S11 and the movie showing snapshots from a simulation trajectory with  $f^a = 30$  and  $\kappa = 10^4$ ). The defect algorithm cannot distinguish between configurations

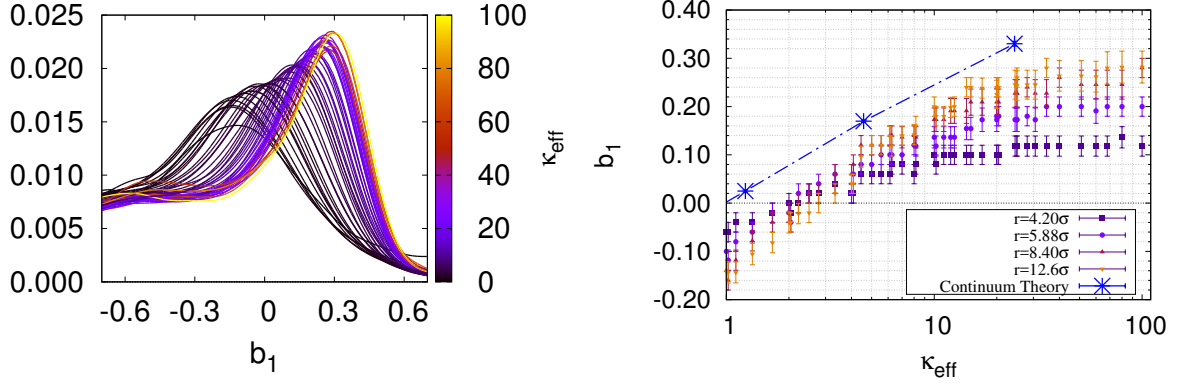


FIG. S14. **(left)** Normalized distributions of  $b_1$  obtained from the simulations in Fig. 3 (main text), with parameterizations calculated at a distance  $r = 12.6\sigma$  from the center of each defect according to Eq. (S10). **(right)** Effect of varying  $r$  (the distance from the center of the  $+1/2$  defect core) on the defect shape parameter  $b_1$ . The mode of  $b_1$  is shown as a function of  $\kappa_{\text{eff}}$  for the simulations in Fig. 3 (main text), with indicated values of  $r$ .

in which stiff rods trans-pierced these holes and actual defects. Therefore we have not measured defect densities for these parameter sets.

- 
- [1] J. D. Weeks, D. Chandler, and H. C. Andersen, *J. Chem. Phys.* **54**, 5237 (1971).  
[2] K. Kremer and G. S. Grest, *J. Chem. Phys.* **92**, 5057 (1990), <http://dx.doi.org/10.1063/1.458541>.  
[3] S. Plimpton, *J. Comput. Phys.* **117**, 1 (1995).  
[4] F. Peruani, A. Deutsch, and M. Bär, *Phys. Rev. E* **74**, 030904 (2006).  
[5] S. R. McCandlish, A. Baskaran, and M. F. Hagan, *Soft Matter* **8**, 2527 (2012).  
[6] S. Weitz, A. Deutsch, and F. Peruani, *Phys. Rev. E* **92**, 012322 (2015).  
[7] F. Ginelli, F. Peruani, M. Bär, and H. Chaté, *Phys. Rev. Lett.* **104**, 184502 (2010).  
[8] F. Peruani, J. Starruß, V. Jakovljevic, L. Søgaard-Andersen, A. Deutsch, and M. Bär, *Phys. Rev. Lett.* **108**, 098102 (2012).  
[9] A. A. Joshi, J. K. Whitmer, O. Guzmán, N. L. Abbott, and J. J. de Pablo, *Soft Matter* **10**, 882 (2014).  
[10] M. Doi and S. Edwards, *The Theory of Polymer Dynamics*, International series of monographs on physics (Clarendon Press, 1988).  
[11] H. H. Wensink, J. Dunkel, S. Heidenreich, K. Drescher, R. E. Goldstein, H. Lowen, and J. M. Yeomans, *Proc. Nat. Acad. Sci. U.S.A.* **109**, 14308 (2012), 1208.4239v1.  
[12] R. Chatterjee, A. A. Joshi, and P. Perlekar, *Phys. Rev. E* **94**, 022406 (2016), arXiv:1608.01142.  
[13] S. Mishra and S. Ramaswamy, *Phys. Rev. Lett.* **97**, 090602 (2006).  
[14] H. Chaté, F. Ginelli, and R. Montagne, *Phys. Rev. Lett.* **96**, 180602 (2006).  
[15] S. Ngo, A. Peshkov, I. S. Aranson, E. Bertin, F. Ginelli, and H. Chaté, *Phys. Rev. Lett.* **113**, 038302 (2014), arXiv:1312.1076.  
[16] E. Putzig and A. Baskaran, *Phys. Rev. E* **90**, 042304 (2014), 1057984.  
[17] X.-q. Shi and Y.-q. Ma, *Nat. Comm.* **4**, 3013 (2013).  
[18] S. Ramaswamy, R. A. Simha, and J. Toner, *Europhys. Lett.* **62**, 196 (2003).  
[19] V. Narayan, S. Ramaswamy, and N. Menon, *Science* **317**, 105 (2007).  
[20] H. P. Zhang, A. Be'er, E.-L. Florin, and H. L. Swinney, *Proc. Natl. Acad. Sci. U. S. A.* **107**, 13626 (2010), <http://www.pnas.org/content/107/31/13626.full.pdf>.  
[21] S. J. DeCamp, G. S. Redner, A. Baskaran, M. F. Hagan, and Z. Dogic, *Nat. Mater.* **14**, 1110 (2015).  
[22] A. J. Vromans and L. Giomi, *Soft Matter*, **1** (2015), 1507.05588.  
[23] S. Zhou, S. V. Shiyankovskii, H.-S. Park, and O. D. Lavrentovich, *Nat. Commun.* **8**, 14974 (2017).